We are IntechOpen,
the world's leading publisher of
Open Access books
Built by scientists, for scientists

6,900
Open access books available

186,000
International authors and editors

200M
Downloads

Our authors are among the

154
Countries delivered to

TOP 1%
most cited scientists

12.2%
Contributors from top 500 universities

CLARIVATE ANALYTICS
BOOK CITATION INDEX
INDEXED

WEB OF SCIENCE™

Selection of our books indexed in the Book Citation Index
in Web of Science™ Core Collection (BKCI)

Interested in publishing with us?
Contact book.department@intechopen.com

Numbers displayed above are based on latest data collected.
For more information visit www.intechopen.com

Tunable Single-, Dual- and Multi-wavelength Fibre Lasers by Using Twin Core Fibre-based Filters

Guolu Yin, Xin Wang, Shuqin Lou and Yiping Wang

Additional information is available at the end of the chapter

Abstract

Tunable fibre lasers draw intensive attention because their emission wavelength can be systematically tuned within a certain spectral range, which allows using a single laser source instead of several sources. This is convenient and cost-effective for many applications in a range of fields, such as telecom, material processing, microscopy, medicine and imaging and so on. The laser wavelength can be tuned in a certain range of wavelength by inserting wavelength-selective elements into the laser's optical cavity. This chapter describes the twin core fibre (TCF)-based filters, which work as the wavelength-selective element. They are introduced into the ring cavity to implement tunable single-, dual- and multi-wavelength fibre lasers. First, we deduced the coupled-mode theory of TCF-based filter. Second, we experimentally and numerically characterized the optical properties of TCF-based filters including free spectral range, polarization dependence, strain effect and bending effect. Finally, we investigated three tunable fibre lasers which operate at single-, dual- and multi-wavelengths, respectively. The operation mechanism of the fibre lasers mainly involved the elastic-optic effect, polarization hole burning effect and non-linear optical loop mirror. We emphasized the tuning mechanism and the tuning characteristics of the tunable fibre lasers.

Keywords: Tunable fibre laser, Twin core fibre, Elastic-optic effect, Polarization hole burning effect, Non-linear optical loop mirror

1. Introduction

Tunable fibre lasers draw serious attention because their emission wavelength can be systematically tuned within a certain spectral range, which allows using a single laser source instead of several sources. This is convenient and cost-effective for many applications in a range of fields, such as telecom, material processing, microscopy, medicine and imaging and so on.

Especially in a wavelength division multiplexing system, the tunable laser is recognized as a backup light source for fixed wavelength laser replacement, with the motivating factors being cost savings and potentially higher system reliability.

Tuning the laser wavelength across a certain wavelength range can be achieved by placing wavelength-selective elements into the laser's optical cavity to provide a particular wavelength selection. Free space filters based on opto-VLSI processor [1] or two-dimensional (2D) dispersion arrangements [2] have been used as wavelength-selective elements for realizing tunable fibre lasers. These filters can provide relatively small tuning steps. However, these devices often suffer from high insertion loss which results in a low side-mode suppression ratio (SMSR). By contrast, in-line fibre filters have been widely used in the laser cavity due to the advantages of low insertion loss, compactness and integration in all fibre laser systems. Conventional Fibre Bragg gratings (FBGs) in single-mode fibres have been used for realizing tunable single-wavelength fibre lasers by highly stretching or bending the FBGs in the laser cavity [3, 4]. Various special fibre-grating structures have been designed to implement dual-wavelength fibre lasers, including a pair of identical FBGs [5], polarization maintained FBGs [6], multimode FBGs [7] and phase-shifted FBGs [8]. Besides the FBGs, a series of modal interferometers draws more attention on tunable single-wavelength fibre lasers due to their easy fabrication and low cost. These modal interferometers can be constructed by using fibre tips [9], two tapers [10, 11], and multimode fibres [12, 13]. High-birefringence Sagnac loop mirrors (HiBi-SLMs) [14, 15] and Lyot birefringence filters [16] were also employed to provide C- and L-band tunable fibre lasers. The modal interferometers and HiBi-SLMs usually lead to polarization hole burning effect which can weaken the homogeneous gain broadening of the erbium-doped fibre (EDF) and help to understand multi-wavelength fibre lasers. Generally, these lasers were switched to operate in dual-/three-wavelength oscillation by adjusting the polarization controllers (PCs). More effective mode suppression techniques have been exploited to obtain more wavelength emissions at room temperature, including phase modulation [17], four-wave mixing [18], Raman scattering [19], Brillouin scattering [20, 21] and a non-linear optical loop mirror (NOLM) [22, 23].

In this chapter, twin core fibre (TCF)-based filters acting as the wavelength-selective element are proposed to achieve tunable single-, dual- and multi-wavelength erbium-doped fibre lasers. This chapter is structured as follows: in Section 1, we will give an overview of the recent development in tunable fibre lasers; in Section 2, we will give the coupled-mode theory of TCF-based filter; in Section 3, we will characterize the optical properties of TCF-based filter, both experimentally and numerically; in Section 4, we will introduce three tunable fibre lasers which operate at single-, dual- and multi-wavelengths, respectively and the conclusion will be given in the fifth section.

2. Coupled-mode theory

The TCF used in our experiments was fabricated by means of the groove-stack-and-draw method. The TCF preform was first prepared by side grooving in a large-diameter pure silica

rod; then the rectangular groove was filled with two small-diameter Ge-doped silica rods and some other small-diameter pure silica rods; finally the rods were fixed in a pure silica jacket tube. Figure 1(a), (b) and (c) illustrates the original preform, micrograph image of the TCF cross section and the magnified micrograph image of the core region, respectively. The diameters of the core and cladding are approximately 6.4 μm and 130 μm, respectively. The separation between the two core axes is 14.2 μm. The difference of the refractive index between the core and cladding is $\Delta = 0.296\%$. We intended to fabricate a TCF with two identical cores. Unfortunately, the two cores in the fabricated TCF have a tiny difference in the geometry shape. In order to evaluate the optical properties accurately, we applied a digital image processing technology to model and rebuild the geometry of the TCF [24], as shown in Figure 1(d). The rebuilt TCF will be used in the numerical analyses in Section 3.
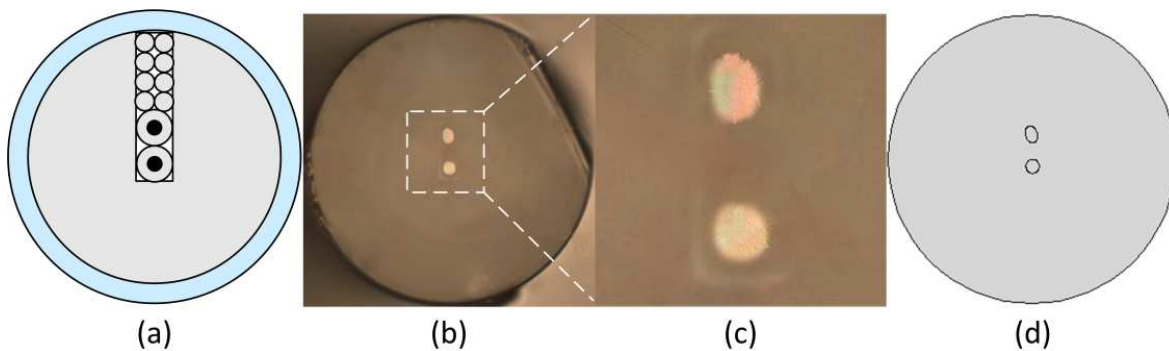

Figure 1. (a) Cross section of the original preform, (b) micrograph image of the TCF cross section, (c) magnified micrograph image of the core region in the TCF, (d) rebuilt geometry of the TCF.

In TCF, light couples back and forth between the two cores. Assuming that light launches into core 1, output amplitude of core 1 can be characterized by using the mode-coupled theory with symmetric and anti-symmetric mode [25]:

$$A^{x,y}(L_0) = \left[\cos\left(S^{x,y}L_0\right) + j\frac{\delta^{x,y}}{S^{x,y}}\sin\left(S^{x,y}L_0\right)\right] \times \exp\left(-j\delta^{x,y}L_0\right) \tag{1}$$

$$\begin{cases} S^{x,y} = \dfrac{\pi}{\lambda}\left(n_e^{x,y} - n_o^{x,y}\right) = \sqrt{\left(\delta^{x,y}\right)^2 + K^2} \\[2mm] \delta^{x,y} = \dfrac{\pi}{\lambda}\left(n_2^{x,y} - n_1^{x,y}\right) = \dfrac{\beta_2^{x,y} - \beta_1^{x,y}}{2} \end{cases} \tag{2}$$

where λ is the wavelength of light in a vacuum, L_0 is the length of the TCF, n_e and n_o are the effective refractive indices (ERIs) of the symmetric and anti-symmetric mode, respectively, n_1 and n_2 are the ERIs of the two cores when the modes in the two cores propagate independently, β_1 and β_2 are the corresponding propagation constants of core 1 and core 2, K is the coupling

coefficient between the fundamental modes of two cores and superscripts x and y represent two orthogonal polarization states.

For a normalized incident light with a given state of polarization (SOP), the electric field can be given as 2D-column vector:

$$E_{in} = \begin{pmatrix} \cos\theta \\ \sin\theta \end{pmatrix} \qquad (3)$$

where θ is the angle between the polarization direction of the incident light and the x-polarization direction. The transmission matrix of the TCF can be expressed as

$$T_{TCF} = \begin{pmatrix} A^x & 0 \\ 0 & A^y \end{pmatrix} \qquad (4)$$

Therefore, the output field E_{out} can be analyzed with the following Jones matrix representation:

$$E_{out} = \begin{pmatrix} E_x \\ E_y \end{pmatrix} = T_{TCF} E_{in} = \begin{pmatrix} A^x & 0 \\ 0 & A^y \end{pmatrix} \begin{pmatrix} \cos\theta \\ \sin\theta \end{pmatrix} = \begin{pmatrix} A^x \cos\theta \\ A^y \sin\theta \end{pmatrix} \qquad (5)$$

Substituting Eq. (1) into Eq. (5), the output power in core 1 can be expressed as [26]

$$
\begin{aligned}
P_1(L_0, \lambda) &= (E_x)^2 + (E_y)^2 \\
&= \left[1 - \frac{(S^x)^2 - (\delta^x)^2}{(S^x)^2} \sin^2(S^x L_0) \right] \cos^2\theta \\
&\quad + \left[1 - \frac{(S^y)^2 - (\delta^y)^2}{(S^y)^2} \sin^2(S^y L_0) \right] \sin^2\theta
\end{aligned} \qquad (6)
$$

If two cores have identical refractive index and diameter, the two cores have the same propagation constants which result in $\beta = \beta_1 = \beta_2$, $\delta = 0$ and $S = K$. Thus, Eq. (6) can be rewritten as

$$P_1(L_0, \lambda) = \cos^2(K L_0) \qquad (7)$$

Here, the coupling coefficient K can be expressed as [27]

$$K = \frac{(2\Delta)^{1/2} U^2 K_0\left(\dfrac{Wd}{a}\right)}{aV^3 K_1^2(W)} \tag{8}$$

$$\begin{cases} U = a\sqrt{k_0^2 n_{co}^2 - \beta^2}, \; W = a\sqrt{\beta^2 - k_0^2 n_{cl}^2} \\ V = \sqrt{U^2 + W^2}, \; \Delta = \left(n_{co}^2 - n_{cl}^2\right)\big/\left(2n_{co}^2\right) \end{cases} \tag{9}$$

where $K_0 = 2\pi / \lambda$ is the wavenumber in vacuum at the wavelength λ, a is the core radius, d is the separation between the two core axes, n_{co} and n_{cl} are the refractive indices of the core and cladding, respectively, Δ is the difference between refractive indices of the core and cladding and K_0 and K_1 are the zero order and first order of modified Bessel functions of the second kind, respectively.

3. Characterization of TCF-based filter

The TCF-based filter is formed by splicing a section of TCF between two segments of SMFs as shown in Figure 2(a). The splicing between the TCF and the SMF is carried out by using an Ericsson fusion splicer (FSU 975) in manual operation mode. We used an active monitoring mode to make the SMF align to one core of the TCF. One end of the SMF was connected to a broadband light source, and one end of the TCF was connected to a power meter through a bare fibre adapter. The other ends of the SMF and TCF were placed in fibre holders of the splicer. We manually adjusted the position of the SMF and TCF by driving the motors in the splicer. When the output power reached the maximum value, we concluded that the SMF was aligned to one core of TCF. Then, we adopted a low-power arc to splice the SMF and TCF. Figure 2(b) shows the micrograph image of the splicing joint between TCF and SMF, which indicates that one core of TCF is precisely aligned to the core of SMF.
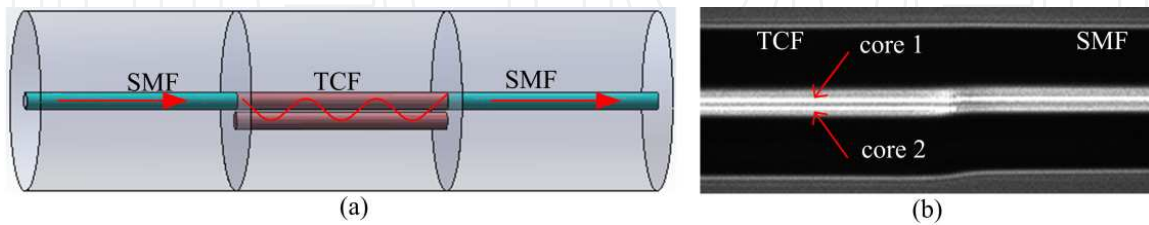

Figure 2. (a) Schematic of a TCF-based filter, (b) micrograph image of the splicing point between TCF and SMF.

Theoretically, we used the finite element method to evaluate the optical properties of TCF. The TCF structure used for numerical calculation is the rebuilt geometry as shown in Figure 1(d). The refractive index of the cladding, n_{cl}, is set as the refractive index of pure silica using

Sellmeier equation and the refractive index of the core is obtained through equation $n_{co} = (1 - 2\Delta^{-1/2})n_{cl}$ with $\Delta = 0.296\%$. At $\lambda = 1550$ nm, n_{co} and n_{cl} are 1.448325 and 1.444023, respectively.

In the following Sections 3.1–3.4, we will investigate four optical properties of TCF-based filters, including free spectra range (FSR), polarization dependence, strain effect and bending effect. All the optical properties are closely related to the tunable fibre lasers discussed in Section 4. In short, the free spectra range mainly determines the tuning range of the fibre laser. The polarization dependence ensures stable dual-wavelength oscillations. The strain effect and bending effect help exactly reflect the tuning mechanism of the fibre lasers.

3.1. Free spectra range

In the TCF-based filter, the light from the SMF is launched into one core of the TCF at the first splicing point. Then, light couples back and forth between the two cores along the TCF. At the second splicing point, a comb-like spectrum was expected according to the coupled-mode theory in Section 2. The transmission dips and peaks occur when the following phase condition is satisfied:

$$\sqrt{\delta^2 + K^2}L_0 = \begin{cases} (m + 1/2)\pi, \text{dip} \\ m\pi, \text{peak} \end{cases} \tag{10}$$

where m is an integer. The separation of the adjacent dips/peaks can be defined as the free spectra range [28]:

$$\Delta\lambda = \frac{\pi/2}{L_0 \dfrac{\partial K}{\partial \lambda}} \tag{11}$$

which indicates that the FSR is inversely proportional to both the length of TCF and the derivative of the coupling coefficient with respect to wavelength.

We fabricated seven TCF-based filters with different length L_0 = 86.9 mm, 115 mm, 160 mm, 250 mm, 0.5 m, 1.1 m and 1.3 m, on the one hand. Light from broadband source (BBS, NKT phonics, superkTM white light laser) is launched into the TCF-based filter and measured by the optical spectrum analyser (OSA, YOKOGAWA, AQ6370C) with a resolution of 0.02 nm. Figure 3(a), (b), (d) and (e) illustrates the transmission spectra of the TCF-based filter with L_0 = 86.9, 115, 160 and 250 mm, respectively. The FSRs of the seven TCF-based filters are measured experimentally to be 49.0, 35.0, 24.2, 15.7, 7.8, 3.7 and 3.2 nm.

On the other hand, we calculated the coupling coefficient K as shown in Figure 3(c), and then calculated the theoretical FSRs through Eq. (11). The experimental FSRs (dashed line) and
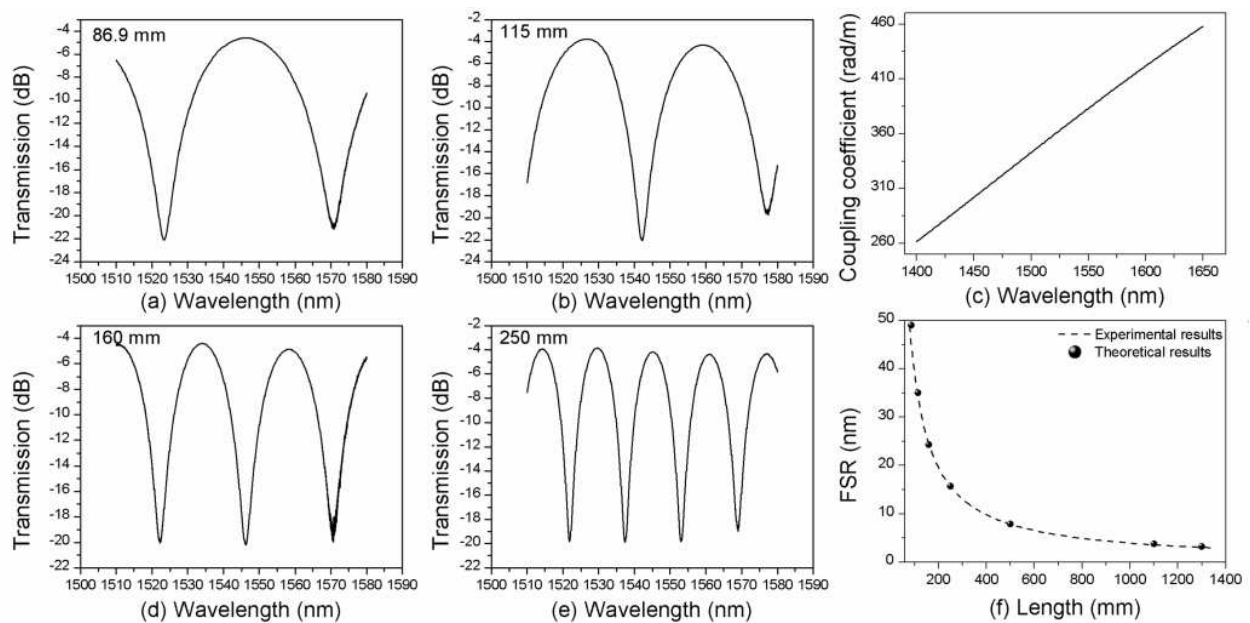
Figure 3. Transmission spectra of TCF-based filters with lengths, L_0, (a) 86.9, (b) 115, (d) 160, (e) 250 mm, (c) calculated coupling coefficient as a function of wavelength, (f) measured and calculated FSRs for various lengths of TCF.

theoretical FSRs (sphere symbols) were illustrated in Figure 3(f). It is found that the experiment results are in accord with the theoretical anticipation.

3.2. Polarization dependence

To theoretically evaluate the polarization dependence of the TCF, we numerically calculated the ERIs of n_e, n_o, n_1 and n_2 as shown in Table 1. Substituting the calculated ERIs into Eq. (2) and combining with Eq. (6), we can obtain the theoretical spectra of the TCF-based filter with different SOPs, as shown in Figure 4(a). It can be found that the position of the transmission peak varies with the SOPs. The theoretical wavelength spacing between the transmission peaks with x-polarization and y-polarization is 1.6 nm. Furthermore, the transmission peaks with SOPs at θ and $(\pi/2-\theta)$ are located symmetrically from each other with respect to the transmission peak with SOP at θ 45°.

In the experiment, we used a polarizer to obtain the linear polarized light from a broadband light source. A polarization controller was used to induce only rotation of this light. Figure 4(b) illustrates the evolution of transmission spectra of the TCF-based filter when the PCF was adjusted. It can be found that the maximum wavelength shift of the transmission peak is 1.2 nm, which is defined as the wavelength spacing between transmission peaks with x-polarization and y-polarization. Such experimental results agree well with the theoretical prediction as shown in Figure 4(a), even though the values of wavelength spacing and the FSR have tiny differences. Two causes can be considered to explain the difference. One is error of the parameters used for the theoretical calculation, including the geometric dimensions and the refractive indexes. The other is the non-uniformity of the homemade TCF in the longitudinal direction. Above all, theoretical and experimental results prove that a TCF-based filter is
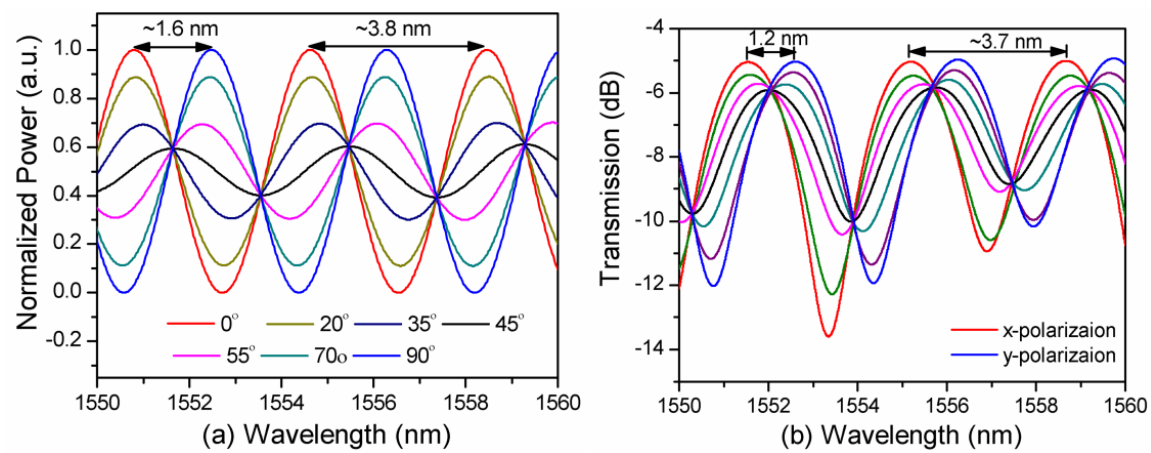
Figure 4. Transmission spectra of the TCF-based filter at different SOPs: (a) theoretical results, (b) experimental results.

polarization dependent. Such polarization dependence induces the polarization hole burning (PHB) effect in the laser cavity and ensures stable dual-wavelength oscillations with tunable wavelength spacing.

ERIs	x-polarization	y-polarization
n_e	1.444855015932922	1.444856531392316
n_o	1.444608454872977	1.444609352306018
n_1	1.444705605736814	1.444705931113986
n_2	1.444787015740477	1.444789030825202

Table 1. Effective refractive indices at λ = 1550 nm.

3.3. Strain effect

As TCF-based filter is applied to axial strain, the refractive index of both core and cladding will decrease according to the photo-elastics [29]:

$$\Delta n_{\text{co/cl}} = -\frac{1}{2} n_{\text{co/cl}}^3 \left[P_{12} - \mu \left(P_{11} + P_{12} \right) \right] \varepsilon_z \tag{12}$$

where ε_z is the axial strain, $P_{11} = 0.12$ and $P_{12} = 0.27$ are the photo-elastic constants for the silica and $\mu = 0.17$ is the Poisson ratio. According to Eq. (12), the decreasing magnitude of the core refractive index is larger than that of the cladding refractive index, which induces a decrease in the refractive index difference between core and cladding. Such a decrease in the refractive index difference would make the electric field of the fundamental core mode extend further to the cladding, thus enhancing the coupling of the two cores, and the coupling coefficient increases as shown in Figure 5(a).

On the other hand, it is worth noting that the coupling coefficients also depend on the wavelength. As the wavelength is increased, the evanescent fields extend further away from the fibre core, the mode overlap increases and as well as the coupling coefficient. As discussed, when the TCF-based filter is stretched, the coupling coefficients would increase because of the elastic–optic effect. In order to keep the phase condition of the transmission peak unchanged in Eq. (10), the wavelength should shift to the short wavelength direction to give an opposite variation of coupling coefficient. Therefore, it is expected to find a 'blue' shift of the transmission peak when the TCF-based filter is stretched.
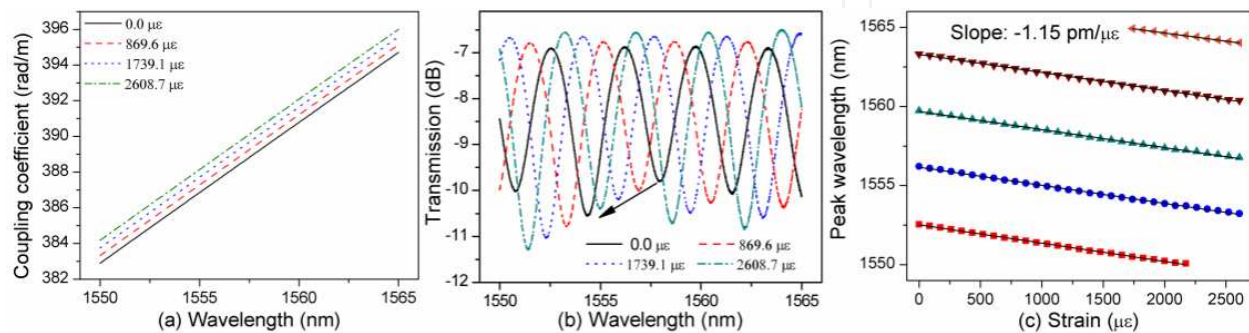

Figure 5. Theoretical and experimental results of TCF-based filter at different axial strains (a) calculated coupling coefficients, (b) transmission spectra of the TCF-based filter, (c) evolution of the peak wavelengths.

To investigate the strain effect experimentally, the TCF-based filter with a TCF length of L_0 = 1.1 m was fixed by two fibre holders adhered to stages. The initial distance between the two stages is around L = 1.15. The fibre was stretched by manually moving the right stage away from the left one, with a 10-µm precision. To qualify the stretching, the displacement of the moving stage is defined as δz which gives rise to an axial strain $\varepsilon_z = \delta z / L$, δz was increased from 0.0 to 3.0 mm with an interval of 0.1 mm. Correspondingly, the axial strain was increased from 0.0 to 2608.7 µε with a step of 86.9 µε. We recorded the transmission spectra of the TCF-based filter at each axial stain. Figure 5(b) illustrates the transmission spectra when $\varepsilon_z = 0$, 869.6, 1739.1, and 2608.7 µε. Figure 5(c) illustrates the evolution of peak wavelength. It can be found that the transmission spectrum shifted toward the shorter wavelength direction. This point agrees with the theoretical prediction implied by the coupling coefficient in Figure 5(a). In detail, the peak wavelength shifts linearly with an increase in axial strain. The sensitivity is around 1.15 pm/ µε.

3.4. Bending effect

Figure 6(a) shows that the TCF is bent with a curvature radius of R. In order to simplify the theoretical calculation, the two cores were assumed to be located in the bend plane. The centre position between two cores is defined as the coordinate zero point. The bending direction is represented by the negative x-direction. Core 1 and core 2 are located in the negative x-direction and positive x-direction, respectively.

When the bending is applied to TCF, the part on outside of the bend (positive x-direction) is in tension, and the part on inside of the bend (negative x-direction) is in compression. According to the elastic–optic effect, the refractive indices of the outside part and inside part in the TCF increase and decrease, respectively. The refractive index profile in the x-direction can be expressed by equivalent refractive index model [30]:

$$n'(x) = n(x)\left(1 + \frac{x}{R}\right) = n(x)(1 + Cx)$$

(13)

where $C = 1/R$ is the curvature and $n(x)$ and $n'(x)$ are refractive index profiles when the TCF is straight and bent, respectively. Figure 6(b) shows the refractive index profile when $C = 0$ and 10 m^{-1}. It can be found that the refractive indices of core 1 and core 2 decrease and increase, respectively.

When the TCF is straight, the two cores have identical refractive index, which results in the same propagation constant $\beta_1 = \beta_2$ at $C = 0$ m^{-1}. When the curvature is gradually increased, the propagation constants of core 1 and core 2 linearly increase and decrease in accordance, respectively, with the refractive index variation of the two cores, as shown in Figure 6(c). As a result, the magnitude of δ in Eq. (10) is increased, as shown in the inset of Figure 6(c).

According to Eq. (10), the phase condition of transmission dips is determined by both δ and K. As discussed, the bending TCF would induce an increase of δ, and a longer wavelength gives larger K as shown in Figure 3(c). In order to keep the phase condition of transmission dip in Eq. (10) unchanged, the wavelength of transmission dips should shift towards the shorter wavelength direction to give an opposite variation of coupling coefficient when TCF is bent. Therefore, a 'blue' wavelength shift of the transmission dip is expected when the TCF-based filter is bent.
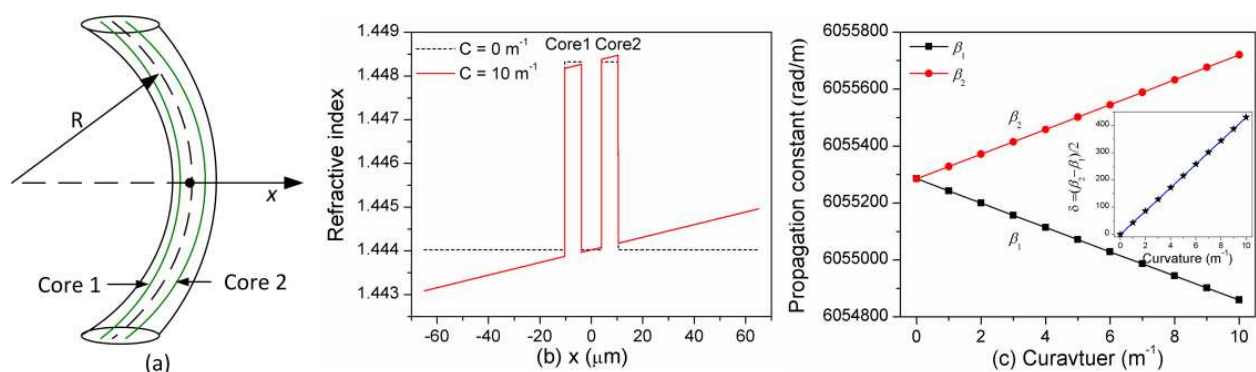

Figure 6. (a) Schematic of a bending TCF, (b) refractive index profile of TCF in x-direction, (c) propagation constants against curvature at $\lambda = 1550$ nm.

Experimentally, we chose the TCF based-filter with a TCF length of $L_0 = 86.9$ mm to evaluate the transmission spectral evolution when the TCF was bent [31]. The TCF-based filter was fixed

by two stages. In order to protect the splice points between TCF and SMF, the stages were placed away from the splice points. Hence, the initial distance between the two stages was L = 103.9 mm. The curvature of the sensor head was adjusted by manually moving one stage towards another one with a 10-µm precision. The bent fibre is normally approximated as an arc of the circle. So the curvature C of the sensor is defined as $C = 1/R = 2h/[h^2+(L/2)^2]$ [32] where h is the displacement at the centre of the TCF-based filter and R is the curvature radius.

Initially, four resonance dips were found at 1461.82, 1510.38, 1558.58 and 1607.90 nm when the TCF-based filter was straight. Figure 7(a) illustrates the evolution of the transmission spectra of the TCF-based filter when its curvature was increased from 0 to 9.3 m^{-1} gradually. It can be found that the spectra shifted towards the shorter wavelength direction, which agrees with the theoretical prospect discussed earlier. Generally, if the curvature is large enough, the resonance dip would shift to the initial position of the adjacent dip, which makes it hard to distinguish the wavelength shift. Therefore, the FSR of the filter generally determines the maximum wavelength shift that can distinguished.
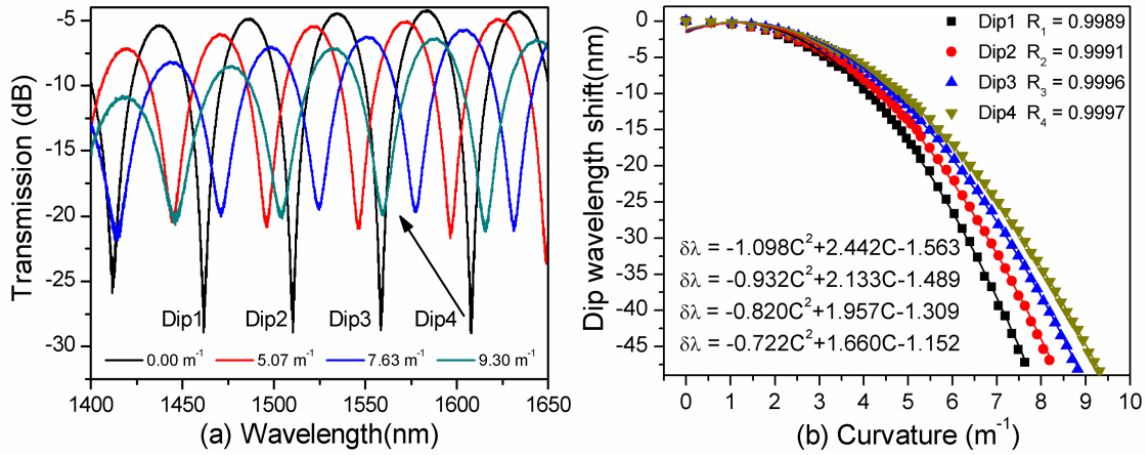

Figure 7. (a) Evolution of transmission spectra of the TCF-based filter, (b) dip wavelength shift against curvature.

Figure 7(b) illustrates the wavelength shift of the four transmission dips; the curvature was increased from 0 to 9.3 m^{-1} gradually. The discrete experimental data can be fitted by a second-order polynomial with an R-square of up to 99.9%. The measurement ranges of the four dips are 7.63, 8.18, 8.82 and 9.30 m^{-1}. It can be found that the resonance dip with a larger resonance wavelength gives rise to a larger measurement range. In addition, the measurement range can be further increased by selecting a shorter TCF, because the FSR is inversely proportional to the TCF length according to Eq. (11).

4. Tunable fibre lasers

The tunable fibre lasers were constructed by using a ring laser cavity as shown in Figure 8(a). A 980-nm diode laser is injected into the laser cavity through a wavelength division multi-

plexor (WDM) to pump the erbium-doped fibre. A polarization-dependent isolator (PDI) is used to ensure that the laser oscillates in a single direction around the ring. The polarization controller is used to adjust the SOP of the light. The laser output is monitored by the optical spectrum analyser (OSA, YOKOGAWA, AQ6370C) from the 5% port of a 95:5 fibre coupler. In the following three subsections, we will investigate three in-line filters to implement the tunable single-, dual- and multi-wavelength fibre lasers.
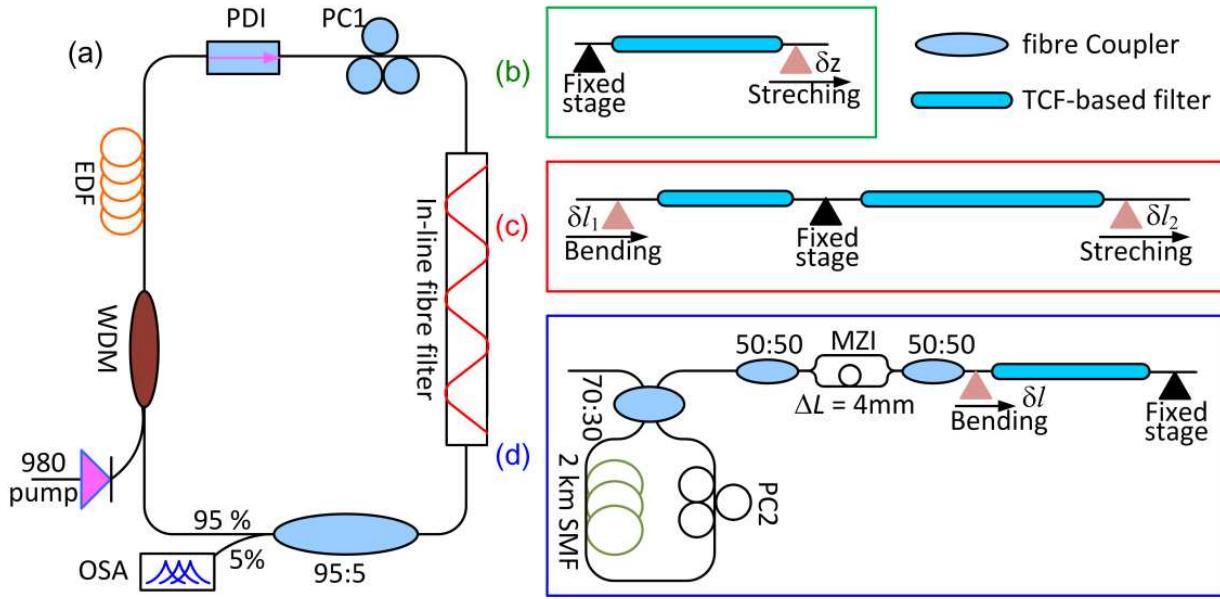

Figure 8. (a) Schematic of the tunable single-, dual- and multi-wavelength fibre lasers; (b), (c) and (d) represent three filters which are used to realize dual-, single- and multi-wavelength fibre lasers. EDF: erbium-doped fibre; WDM: wavelength division multiplexor; PC: polarization controller; PDI: polarization-dependent isolator, OSA: optical spectrum analyser.

4.1. Dual-wavelength and single-polarized fibre laser

In this work, we proposed and experimentally demonstrated a tunable dual-wavelength and single-polarized fibre laser by use of a TCF-based filter [26]. Figure 8(b) illustrates the TCF-based filter with a TCF length, L_0, of 1.1 m. In this section, we first presented the principle of the dual-wavelength fibre laser. Second, we evaluated the tunability of dual-wavelength spacing by adjusting the PC and investigated the lasing wavelength shift by stretching the TCF. Finally, we verified the single-polarized operation of the dual-wavelength fibre laser.

In the dual-wavelength fibre laser, the TCF-based filter simultaneously works as the wavelength selector and the polarization-dependent element. The TCF-based filter gives rise to a comb transmission spectrum. The SOP of the wavelengths is adjusted by using the PC, and the wavelengths with particular SOPs could become transmission peaks according to Figure 4. The polarization dependence of the TCF is helpful for inducing the PHB effect and in turn simultaneously amplifying the particular transmission peaks and achieving stable dual-wavelength oscillation.

At first, a single wavelength was obtained at λ = 1559.2 nm, then the single-wavelength was split into two wavelengths when the PC was slightly adjusted, as shown in Figure 9(a). The dual-wavelength fibre laser has a 3-dB line width of 0.047 nm and an SMSR of 40–52 dB. The maximum difference between the peak powers of the two wavelengths is around 1.2 dB. The wavelength spacing between the two wavelengths can be tuned from 0.1 to 1.2 nm by adjusting the PC.
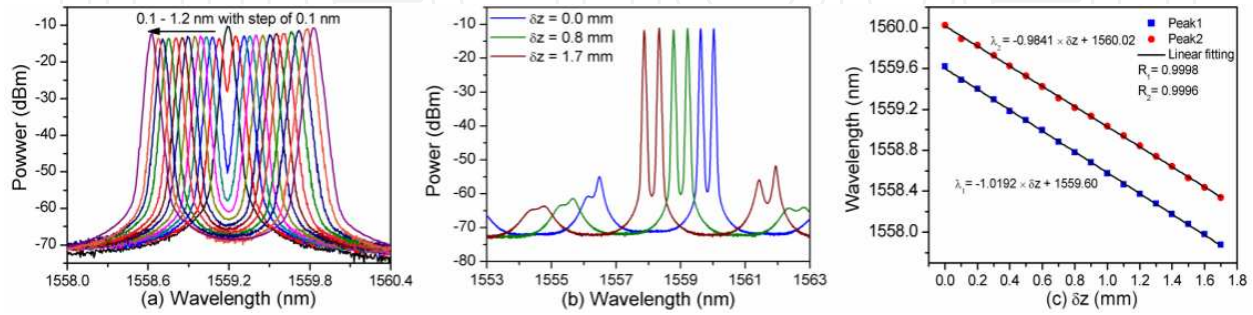

Figure 9. Experimental results of a tunable dual-wavelength fibre laser. (a) wavelength spacing is varied from 0.1 to 1.2 nm, (b) two wavelengths were simultaneously tuned by stretching the TCF, (c) two lasing wavelengths as a function of δz.

For fixed wavelength spacing, the simultaneous tuning characteristic of the dual-wavelength laser was investigated by stretching the TCF-based filter. As discussed in Section 3.3, the transmission spectrum of the TCF-based filter exhibited a 'blue shift' when it was stretched. In contrast, the value of wavelength spacing remained unchanged because the birefringence of the TCF hardly changed. Therefore, we found that the two lasing wavelengths can be simultaneously tuned towards the shorter wavelength with fixed wavelength spacing. Dual-wavelength lasing with wavelength spacing of 0.4, 0.8 and 1.2 nm was linearly tuned over 1.7, 1.0 and 0.8 nm, respectively. Here, we give only the measured results of dual-wavelength lasing with wavelength spacing of 0.4 nm as shown in Figure 9(b). When the TCF was stretched by an increment length of δz = 0.1 mm, two lasing wavelengths simultaneously moved with a step of 0.1 nm, as shown in Figure 9(c).

To study the SOPs of the dual-wavelength output, the laser output was connected to a polarization beam splitter (PBS) through a PC. The x- and y- outputs of the PBS were injected into the OSA to evaluate the dual-wavelength spectrum at two orthogonal polarizations. We adjusted the PC to make the two wavelengths polarize at x-axis and y-axis, respectively. Figure 10(a)–(d) shows the measurement results of dual-wavelength lasing with wavelength spacing of 0.2, 0.4, 0.8 and 1.2 nm. It can be found that the out spectrum at the x-axis or y-axis has only one dominating wavelength, while the other one is substantially suppressed. The cross-polarization suppression between the two wavelengths is more than 30 dB, which means the two wavelengths are orthogonal in polarization and the dual-wavelength laser operated on a single-polarization state.
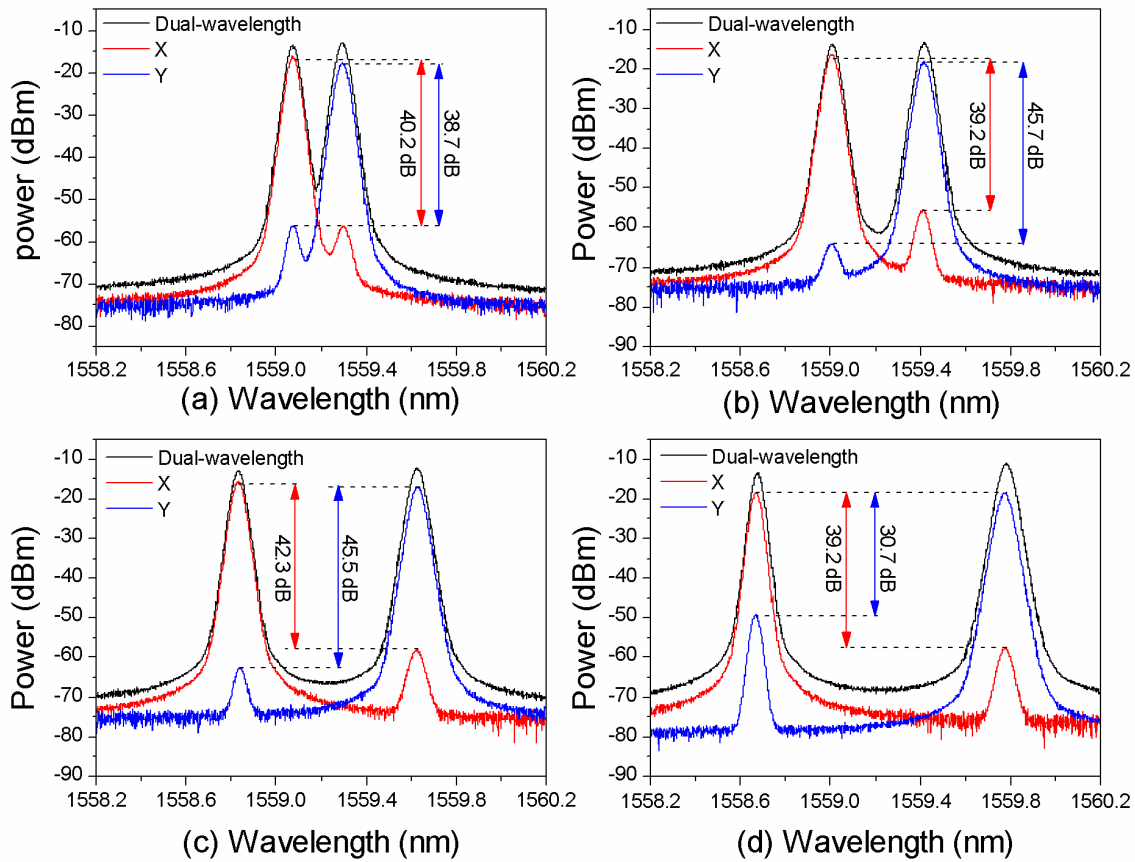
Figure 10. Output spectra of lasers with orthogonal polarization states for wavelength spacing of (a) 0.2 nm, (b) 0.4 nm, (c) 0.8 nm, (d) 1.2 nm.

4.2. Tunable single-wavelength fibre laser

In this work, we proposed and experimentally demonstrated a C-band tunable single-wavelength fibre laser by cascading two TCF-based filters [33]. Figure 8(c) illustrates the cascaded TCF-based filters with TCF lengths of 0.14 and 1.37 m. In this section, we discussed the tuning mechanism by characterizing the two TCF-based filters and investigated the tunable characteristics of the proposed tunable single-wavelength fibre laser by bending one TCF-based filter and stretching the other one.

4.2.1. Tunable mechanism

Figure 11 illustrates the tuning equipment of the cascading TCF-based filters, which consists of three transmission stages. Filter 1 was fixed by the left and middle stages with an initial distance of L_1 = 0.20 m, and filter 2 was fixed by the middle and right stages with an initial distance of L_2 = 1.43 m. The up and mid panels of Figure 12(a) illustrate the transmission spectra of the two individual TCF-based filters, which indicate that the two filters have an FSR of 28.6 and 2.9 nm. The lower panel of Figure 12(a) illustrates the spectrum of the combined structure. It can be found that the output of the cascading filters is a superposition of a slowly varying

envelope with an FSR of 28.6 nm produced by filter 1 and a dense fringe with an FSR of 2.9 nm produced by filter 2.
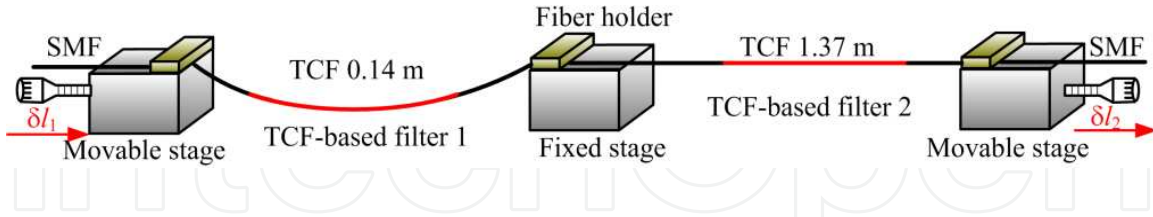

Figure 11. Schematic of the tuning technique of cascading filters.

We coarsely tuned the cascaded spectrum by bending TCF-based filter 1 and finely tuned the spectrum by stretching the TCF-based filter 2. Filter 1 is bent by moving the left stage towards the middle one. The moving distance of the left stage (δl_1) is increased from 0 to 1.9 mm with a step of ~0.25 mm. Figure 12(b) illustrates the evolution of the spectra. It can be found that the dense fringes are nearly located at the same position, and the envelope shifts towards the shorter wavelength. The envelope selects one of the dense peaks as the highest transmission peak (square symbols). The highest transmission peak can be tuned over the wavelength range of 23.2 nm with a coarse step of 2.9 nm which is determined by the FSR of TCF-based filter 2.
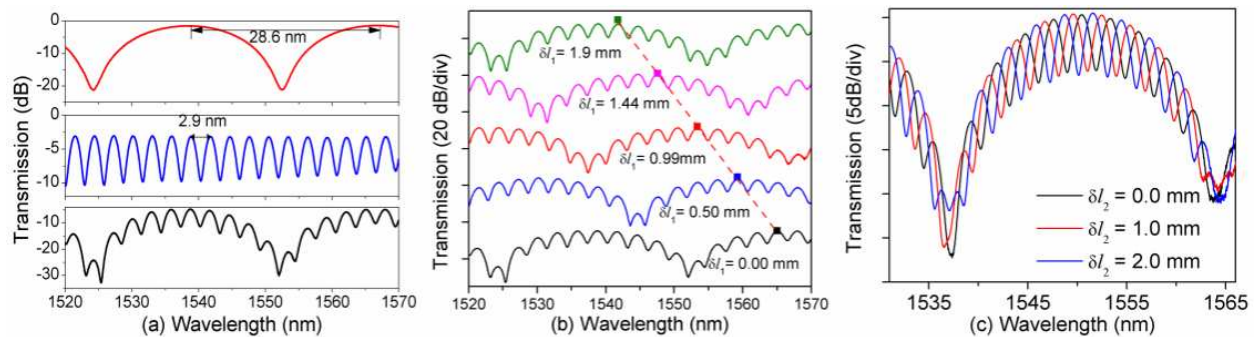

Figure 12. (a) Transmission spectra of TCF-based filter 1 (upper panel), TCF-based filter 2 (mid panel) and cascading filters (lower panel). Transmission spectra evolution of the cascading filters (b) when TCF-based filter 1 is bent and (c) when TCF-based filter 2 is stretched.

In order to realize a fine wavelength tuning, TCF-based filter 2 is stretched by moving the right stage away from the middle one. The moving distance of the right stage (δl_2) is increased from 0 to 3.0 mm with steps of 0.25 mm. Figure 12(c) illustrates the evolution of spectra when we stretched filter 2. It can be found that the envelope almost remains unchanged while the dense fringes shift towards a shorter wavelength. The highest transmission peaks can be finely tuned over the wavelength range of 2.9 nm with a certain fine step which is dependent on the strain applied on filter 2. In conclusion, the envelope and the dense fringes of the transmission spectra can be separately tuned by bending and stretching filters 1 and 2, respectively.

4.2.2. Characterization of tunable laser

The fibre laser was coarsely tuned by bending TCF-based filter 1 and finely tuned by stretching the TCF-based filter. Figure 13(a) illustrates the evolution of lasing spectra when we bent filter 1. It can be found that bending filter 1 makes the envelope shift towards shorter wavelengths and selects the transmission peak of filter 2 for lasing in a series of steps with a separation of 2.9 nm. Figure 13(b) illustrates the evolution of lasing spectra when we stretched filter 2. It was found that the lasing wavelength finely changed with a step of 0.22 nm. Figure 13(c) illustrates the whole tuning process. First, we obtained the initial single-wavelength lasing at 1565.00 nm. Second, we stretched filter 2 from $\delta l_2 = 0$ to 3.0 mm with a step of 0.25 mm and obtained fine lasing wavelengths with a step of ~0.22 nm, e.g. from 1565.04 to 1562.26 nm (black dots). Third, we loosened filter 2 to the initial position and then bent filter 1 with $\delta l_1 = 0.25$ mm (black arrow), and another coarse lasing wavelength was selected for lasing with a separation of 2.9 nm from the last one, e.g. 1562.12 nm. Fourth, the second and third steps were repeated eight times. On further bending filter 1 and stretching filter 2, the lasing wavelength jumped from 1541.8 to 1565.04 nm. Consequently, the wavelength can be linearly tuned over the wavelength range of 23.2 nm (from 1541.8 to 1564.0 nm) with a uniform step of ~0.22 nm. The total number of tunable lasing wavelength is up to 105.
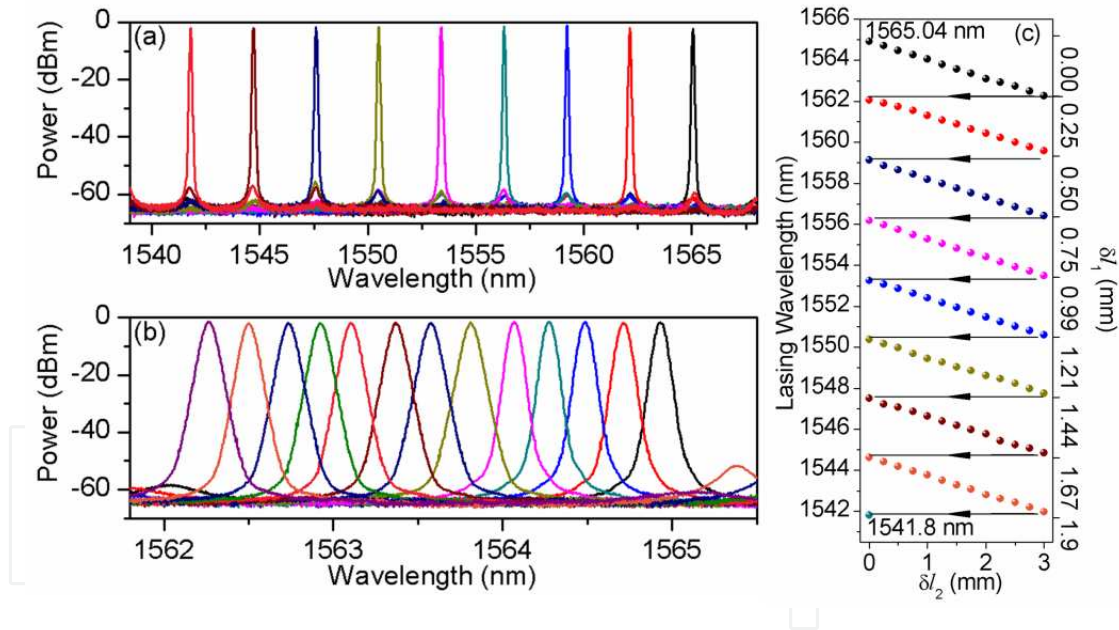

Figure 13. Output of a tunable fibre laser (a) coarse laser lines when TCF-based filter 1 is bent, (b) fine laser lines when TCF-based filter 2 is stretched, (c) all tunable laser wavelength evolution.

When we characterized the laser properties, we increased the pump power from 10 to 500 mW. The cavity loss was around 7 dB including the splicing loss (~4 dB) between the SMF and the TCF and the insertion loss of other optical devices. Such cavity loss gives rise to a threshold pump power of 20 mW. When the pump power was 500 mW, the lasing output saturated at 2.27 dB. Hence, we measured all 105 laser spectra at a pump power of 500 mW. For good visibility, only half of the lasing spectra are plotted in Figure 14. The SMSRs are 53 –58 dB, and
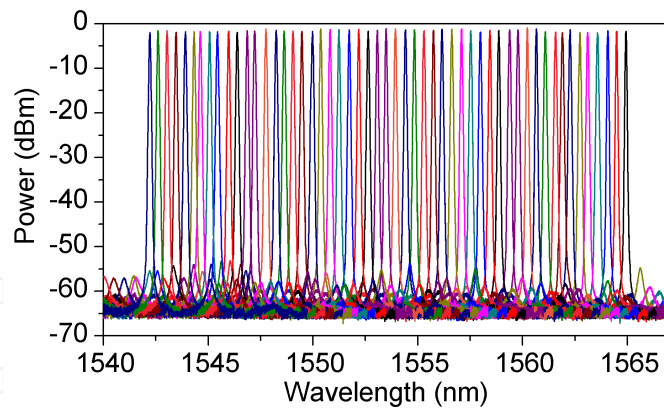
Figure 14. Output of the tunable fibre laser with a range of 23.2 nm and a uniform step of ~0.22 nm.

the linewidth is ~0.05 nm. The intensity variation over the entire tuning range was less than ±0.1 dB.

4.3. Tunable multi-wavelength fibre laser

In this work, we proposed and experimentally demonstrated a tunable multi-wavelength fibre laser based on a non-linear optical loop mirror by using a compound filter [34]. Figure 8(d) illustrates the NOLM and the compound filter. The compound filter was formed by cascading a standard Mach–Zehnder interferometer (MZI) and a TCF-based filter. In this section, we first discussed the function of the NOLM as an amplitude equalizer. Second, we discussed the tuning mechanism by characterizing the transmission spectra of the standard MZI, the TCF-based filter and the compound filter. Third, we investigated the tunable characteristics of the proposed tunable multi-wavelength fibre laser by bending the TCF. Finally, we discussed the influence of the length of the TCF on the laser characteristic.

4.3.1. Non-linear optical loop mirror

An NOLM is formed by splicing together the output ports of a 70:30 coupler. A 2-km SMF is inserted inside the loop. The transmission of the NOLM is given as [23]:

$$T = 1 - 2\rho(1-\rho)\left\{1 + \cos\left[\alpha + (1-2\rho)\phi\right]\right\}$$ (14)

where ρ is the splitting ratio of the coupler, $\phi = 2\pi n_3 P L_3 / (\lambda A_{\text{eff}})$ is the non-linear phase shift induced by the self-phase modulation and cross-phase modulation, n_3 is the non-linear refractive index coefficient, L_3 is the loop length, A_{eff} is the effective fibre core area, λ is the operating wavelength, P is the input power and α is the additional linear phase difference induced by PC2 and the fibre twist.

According to Eq. (14), the transmission of NOLM is a cosine function of the total phase difference and varies with a change in α. When α is set to certain values by adjusting PC2, the NOLM can be biased at the negative feedback regime, and the transmissivity decreases with

the input power. In such a case, the NOLM works as an amplitude equalizer to weaken the homogeneous gain broadening and suppress the mode competition. The multi-wavelength oscillations can be achieved at these particular PC settings.

4.3.2. Tuning mechanism

The standard MZI is established by connecting two 50:50 filters between which the fibre path difference of two arms is ΔL = 4.0 mm. The channel spacing of the standard MZI is ~ 0.4 nm, as shown in the upper panel of Figure 15(a). The mid panel of Figure 15(b) illustrates the transmission spectrum of the TCF-based filter with a TCF length of L_0 =11.5 mm and an FSR of 37 nm. The compound filter is constructed by combining the standard MZI and the TCF-based filter, and its transmission spectrum is shown in the lower panel of Figure 15(c). The fast-varying fine fringe pattern is modulated with a slow-varying one. The higher spatial frequency corresponds to the response of the standard MZI; the red line of the lower spatial frequency corresponds to the response of the TCF-based filter. In other words, the compound filter is a comb filter whose transmission peaks are modified in accordance with the shape of the spectrum of the TCF-based filter.
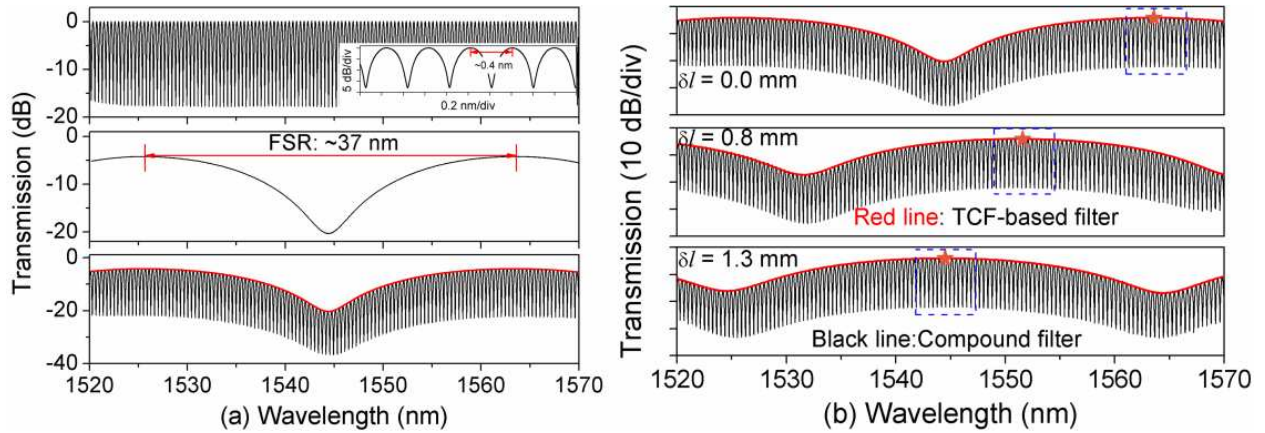

Figure 15. (a) Transmission spectra of the standard MZI (upper panel), the TCF-based filter (mid panel) and the compound filter (lower panel), (b)transmission spectra of the compound filter and the TCF-based filter when the TCF was bent with δl = 0.0, 0.8 and 1.3 mm.

The compound filter was tuned by bending the TCF. The TCF-based filter was fixed by two fibre holders adhered onto two stages with an initial distance of 25 cm. The filter was bent by moving the right stage towards the left one. To quantify the bending of the filter, we recorded the displacement of the moving stage; the initial position of the moving stage is defined as the zero point δl = 0.0 mm. Figure 15(b) illustrates the transmission spectra of the TCF-based filter (red lines) and the compound filter (black lines) when δl = 0.0, 0.8 and 1.3 mm. It can be found that the transmission peak (pentagram symbols) of TCF-based filters exhibits a 'blue shift' when δl is gradually increased. Because the transmissivity of the individual transmission peak of the standard MZI is modulated by the variation spectra of the TCF-based filter, the envelopes of the spectra of the compound filter also exhibit a 'blue shift'. In other words, the compound

filter is tuned by moving its envelope towards the short-wavelength direction by bending the TCF.

The principle of the proposed tunable multi-wavelength fibre laser can be expressed as follows. The ASE spectrum of the EDF is reshaped to a comb-like transmission spectrum by the standard MZI. The intensities of the transmission peaks are modified by the TCF-based filter. Because lasing is established once the cavity loss is smaller than the EDF gain, only the peaks with high transmissivity (low loss) can oscillate. The transmission peak of TCF-based filter has the lowest insertion loss; hence, only the near region of the transmission peak would be selected for lasing simultaneously, as shown in the blue region of Figure 15(b). The wavelength range of the blue region is determined by the balance between the EDF gain profile and the profile of the total cavity loss. The NOLM can work as an amplitude equalizer to enable the multiple transmission peaks to emit as lasing wavelengths. When the TCF is bent, the transmission band of the TCF-based filter shifts towards the short-wavelength direction to cover the different channels provided by the standard MZI. Thus, the corresponding multiple lasing lines shift towards the short-wavelength direction. As a result, a tunable multi-wavelength fibre laser is realized by bending the TCF.

4.3.3. Laser tunable characterization

To study the tuning characteristic, the moving stage was adjusted with a step of 0.05 mm. Figure 16(a) illustrates that the lasing wavebands can be continuously tuned to cover a range of 24 nm from 1542 to 1566 nm. The lasing spectra were measured when the TCF was bent with δl = 0.0, 0.3, 0.8 and 1.3 mm (labelled 1–4, respectively). In the 3-dB spectral range, the lasing line amount in each lasing spectrum is around 12 peaks at least and 19 peaks at most.
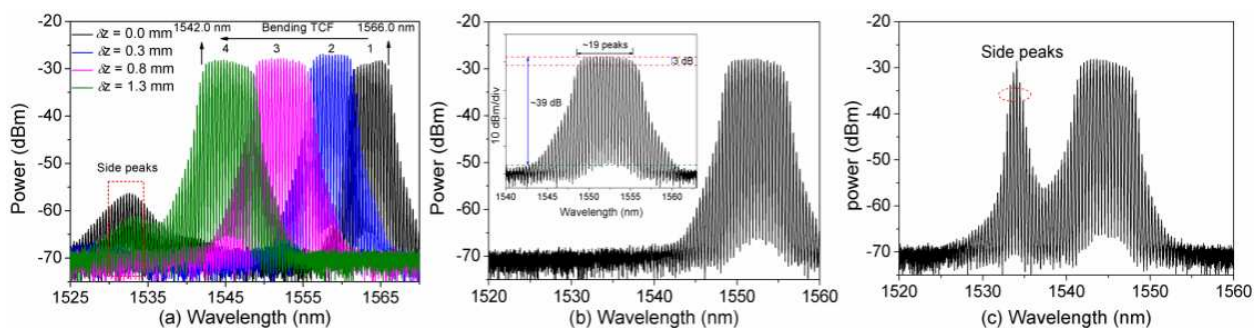

Figure 16. Lasing spectra of the multi-wavelength fibre laser (a) tunable characteristic, (b) the TCF was bent with δl = 0.8 mm and (c) δl =1.35 mm.

When δl = 0.0 mm, because the transmission peaks around 1532 nm have considerable intensities, the lasing spectrum 1 exhibits side modes around 1532 nm. Because the total fixed gain is shared by both side peaks and the lasing peaks, the lasing line amount is limited to 12 peaks in the lasing spectrum 1. When the TCF was bent, the transmission band of the TCF-based filter shifted towards the shorter wavelength direction and supressed the transmission peaks around 1532 nm, as shown in Figure 15(b). When δl is in the range from 0.4 to 0.9 mm,

the transmission dip of the TCF-based filter locates around 1532 nm, resulting in transmission peaks with relatively low transmissivities. Thus, the side peaks can be efficiently suppressed. Taking δl = 0.8 mm, for example, the spectrum of the compound filter is shown in Figure 15(b), and the corresponding lasing spectrum is shown in Figure 16(b). The lasing lines are enlarged in the inset of Figure 16(b). It can be found that 19 lasing lines are located in the 3-dB spectral range. All lasing lines have an SMSR of 39 dB, a peak power of −28 dBm and a channel spacing of 0.4 nm. When we increased δl to 1.3 mm, the transmissivities of the peaks around 1532 nm increased as shown in Figure 15(b), which induced an increment of the side peaks in the laser output, as shown in the laser spectrum 4 of Figure 16(a). When we continually increased δl to 1.35 mm, the side peaks increased dramatically, as shown in Figure 16(c). As a result, we concluded that the side peaks induced by the EDF peak gain mainly limited the tuning range of the proposed laser.
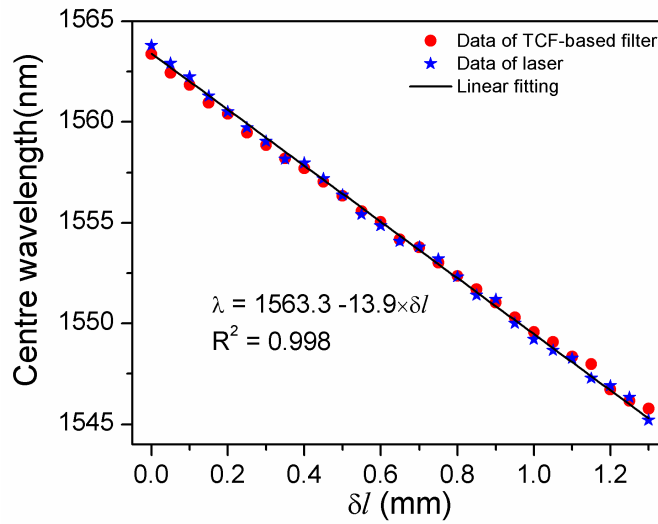

Figure 17. Centre of the lasing waveband and the transmission peak of the TCF-based filter as a function of δl.

In order to find out the relationship between the transmission spectrum of the TCF-based filter and multi-wavelength lasing spectrum, we plotted both the transmission peak of the TCF-based filter (blue pentagram symbols) and the centre of the lasing waveband (red circle symbols) as a function of δl, as shown in Figure 17. It seems that the centre of the lasing waveband tracks the transmission peak of the TCF-based filter. This point proves that the tuning mechanism of the proposed tunable fire laser takes advantage of the variation transmission band of the TCF-based filter to select different channels of the standard MZI for realizing a tunable lasing waveband.

4.3.4. Influence of the TCF length on the tuning characteristic

In order to investigate the influence of the TCF length on the tuning characteristic, we fabricated two more filters with a TCF length of L_0 = 5.0 and 22 cm. Figure 18(a) illustrates the

tuning characteristic of the multi-wavelength fibre based on the TCF-based filter with a TCF length of L_0 = 5.0 cm. The results indicate that the lasing waveband covers a range of 15.2 nm from 1548.0 to 1563.2 nm. The lasing line amount in each lasing spectrum is around 18 peaks at the lowest and 25 peaks at the highest. Compared with the case of L_0 = 11.5 cm, the tuning range decreased by 8.8 nm, and the lasing line amount increased by six peaks. To explain the difference, we measured the transmission spectrum of the TCF-based filter with L_0 = 5.0 cm, as shown in the inset of Figure 18(a). It can be found that the FSR of the filter is 84 nm which means it is difficult for such a large FSR to suppress the side peaks around 1532 nm. Therefore, the tuning range limited by the side peaks is decreased when we increased the length of the TCF. On the contrary, the large FSR also means a flat transmission waveband, which increased the lasing line amount.
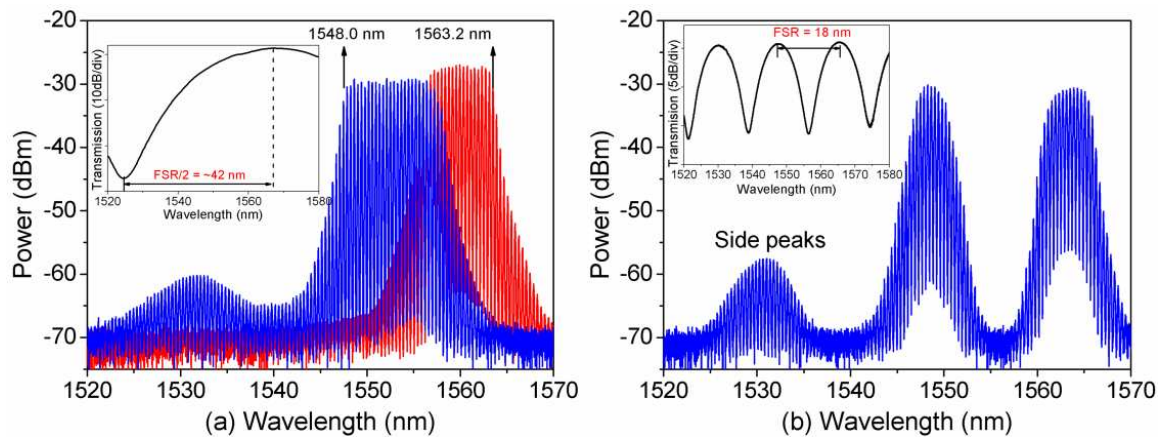

Figure 18. Lasing spectra of the proposed tunable multi-wavelength fibre laser with TCF lengths (a) L_0 = 5 cm and (b) L_0 = 22 cm. Inset: the transmission spectra of the TCF-based filter.

We carried out a reverse experiment by using a large length of TCF with L_0=22 cm. Figure 18(b) illustrated the lasing spectrum. It can be found that two lasing wavebands oscillated simultaneously. To explain the two lasing wavebands, we also measured the transmission spectrum of the TCF-based filter, as shown in the inset of Figure 18(b). It can be found that two transmission wavebands are located in the spectrum, which results in two lasing wavebands. Because the two bands shared the EDF gain, the SMSR of the lasing spectrum is drastically decreased to 21 dB. Summarizing the multi-wavelength fibre laser with TCF lengths of L_0=5.0, 11.5 and 22 cm, we can conclude that there is balance between the tuning range and the lasing line amount when we choose the length of the TCF. The shorter the TCF length, the narrower the tuning range and the larger the number of the lasing wavelengths.

5. Conclusion

In this chapter, we studied tunable single-, dual- and multi-wavelength fibre lasers by using TCF-based filters. First, we presented the coupled-mode theory of the TCF with symmetric and anti-symmetric mode and deduced the output of the TCF-based filter on the basis of the

SOP of input light. Second, we experimentally and numerically characterized the optical properties of TCF-based filter including the free spectral range, polarization dependence, strain effect and bending effect. These optical properties are closely related to the tuning mechanism and tuning characteristics of the tunable fibre lasers. Third, we implemented three tunable fibre lasers which operate at single-, dual- and multi-wavelengths, respectively. In the case of a tunable single wavelength, the wavelength can be linearly tuned over 23.2 nm (from 1541.8 to 1564.0 nm), with a uniform step of ~0.22 nm. The total number of tunable wavelength is up to 105. In the case of a tunable dual-wavelength fibre laser, the single-polarized two wavelengths can be linearly tuned by stretching the TCF. The spacing of the two wavelengths can be tuned from 0.1 to 1.2 nm by adjusting the PC located before the TCF-based filter. In the case of a tunable multi-wavelength fibre laser, 19 wavelengths were tuned over 24 nm from 1542 to 1566 nm. After discussing the influence of the TCF length on the tunable multi-wavelength fibre laser, it is concluded that there is balance between the tuning range and the wavelength amount when we choose the length of the TCF.

Acknowledgements

Author details

Guolu Yin[1], Xin Wang[2], Shuqin Lou[2] and Yiping Wang[1]

*Address all correspondence to: guoluyin@gmail.com

1 Key Laboratory of Optoelectronic Devices and Systems of Ministry of Education and Guangdong Province, College of Optoelectronic Engineering, Shenzhen University, Shenzhen, China

2 School of Electronic and Information Engineering, Beijing Jiaotong University, Beijing, China

References

[1] Xiao F, Alameh K, Lee T. Opto-VLSI-based tunable single-mode fiber laser. Optics Express. 2009; 17(21): 18676–18680. DOI: 10.1364/OE.17.018676

[2] Sinefeld D, Marom DM. Tunable fiber ring laser with an intracavity high resolution filter employing two-dimensional dispersion and LCoS modulator. Optics Letters. 2012; 37(1): 1–3. DOI: 10.1364/OL.37.000001

[3] Song YW, Havstad SA, Starodubov D, Xie Y, Willner AE, Feinberg J. 40-nm-wide tunable fiber ring laser with single-mode operation using a highly stretchable FBG. IEEE Photonics Technology Letters. 2001; 13(11): 1167–1169. DOI: 10.1109/68.959352

[4] Babin SA, Kablukov SI, Vlasov AA. Tunable fiber Bragg gratings for application in tunable fiber lasers. Laser Physics. 2007; 17(11): 1323–1326. DOI: 10.1134/s1054660x07110096

[5] He X, Fang X, Liao C, Wang D, Sun J. A tunable and switchable single-longitudinal mode dual-wavelength fiber laser with a simple linear cavity. Optics Express. 2009; 17(24): 21773–21781. DOI: 10.1364/OE.17.021773

[6] Feng SC, Xu O, Lu SH, Mao XQ, Ning TG, Jian SS. {PT ArticleTitle}Single-polarization, switchable dual-wavelength erbium-doped fiber laser with two polarization-maintaining fiber Bragg gratings. Optics Express. 2008; 16(16): 11830–11835. DOI: 10.1364/OE.16.011830

[7] Feng X, Liu Y, Yuan S, Kai G, Zhang W, Dong X. L-Band switchable dual-wavelength erbium-doped fiber laser based on a multimode fiber Bragg grating. Optics Express. 2004; 12(16): 3834–3839. DOI: 10.1364/OPEX.12.003834

[8] Villanueva GE, Perez-Millan P, Palaci J, Cruz JL, Andres MV, Marti J. Dual-wavelength DFB erbium-doped fiber laser with tunable wavelength spacing. IEEE Photonics Technology Letters. 2010; 22(4): 254–256. DOI: 10.1109/lpt.2009.2038594

[9] Wang XZ, Li Y, Bao XY. Tunable ring laser using a tapered single mode fiber tip. Applied Optics. 2009; 48(35): 6827–6831. DOI: 10.1364/AO.48.006827

[10] Wang XZ, Li Y, Bao XY. C- and L-band tunable fiber ring laser using a two-taper Mach-Zehnder interferometer filter. Optics Letters. 2010; 35(20): 3354–3356. DOI: 10.1364/OL.35.003354

[11] Yin GL, Wang XZ, Bao XY. Effect of beam waists on performance of the tunable fiber laser based on in-line two-taper Mach-Zehnder interferometer filter. Applied Optics. 2011; 50(29): 5714–5720. DOI: 10.1364/AO.50.005714

[12] Antonio-Lopez JE, Castillo-Guzman A, May-Arrioja DA, Selvas-Aguilar R, LiKamWa P. Tunable multimode-interference bandpass fiber filter. Optics Letters. 2010; 35(3): 324–326. DOI: 10.1364/OL.35.000324

[13] Castillo-Guzman A, Antonio-Lopez JE, Selvas-Aguilar R, May-Arrioja DA, Estudillo-Ayala J, LiKamWa P. Widely tunable erbium-doped fiber laser based on multimode interference effect. Optics Express. 2010; 18(2): 591–597. DOI: 10.1364/OE.18.000591

[14] Sun GY, Zhou YW, Hu YH, Chung Y. Broadly tunable fiber laser based on merged Sagnac and intermodal interferences in few-mode high-birefringence fiber loop mir-

ror. IEEE Photonics Technology Letters. 2010; 22(11): 766–768. DOI: 10.1109/lpt.2010.2044991

[15] Zhou YW, Sun GY. Widely tunable erbium-doped fiber laser based on superimposed core-cladding-mode and Sagnac interferences. IEEE Photon Journal. 2012; 4(5): 1504–1509. DOI: 10.1109/jphot.2012.2211074

[16] Zhang J, Qiao XG, Liu F, Weng YY, Wang RH, Ma Y, Rong QZ, Hu ML, Feng ZY. A tunable erbium-doped fiber laser based on an MZ interferometer and a birefringence fiber filter. Journal of Optics. 2012; 14(1): 015402. DOI: 10.1088/2040-8978/14/1/015402

[17] Luo AP, Luo ZC, Xu WC. Tunable and switchable multiwavelength erbium-doped fiber ring laser based on a modified dual-pass Mach-Zehnder interferometer. Optics Letters. 2009; 34(14): 2135–2137. DOI: 10.1364/OL.34.002135

[18] Harun SW, Parvizi R, Shahi S. Multi-wavelength erbium-doped fiber laser assisted by four-wave mixing effect. Laser Physics Letters. 2009; 6(11): 813–815. DOI: 10.1002/lapl.200910072

[19] Wang ZY, Cui YP, Yun BF, Lu CG. Multiwavelength generation in a Raman fiber laser with sampled Bragg grating. IEEE Photonics Technology Letters. 2005; 17(10): 2044–2046. DOI: 10.1109/LPT.2005.856430

[20] Zhang Z, Zhan L, Xia YX. Tunable self-seeded multiwavelength Brillouin-erbium fiber laser with enhanced power efficiency. Optics Express. 2007; 15(15): 9731–9736. DOI: 10.1364/OE.15.009731

[21] Peng WJ, Yan FP, Li Q, Yin GL, Feng SC, Feng T, Tan SY. Tunable self-seeded multiwavelength Brillouin–erbium fiber laser using an in-line two-taper Mach–Zehnder interferometer. Optics & Laser Technology. 2013; 45: 348–351. DOI: 10.1016/j.optlastec.2012.06.025

[22] Tran TVA, Lee K, Lee SB, Han YG. Switchable multiwavelength erbium doped fiber laser based on a nonlinear optical loop mirror incorporating multiple fiber Bragg gratings. Optics Express. 2008; 16(3): 1460–1465. DOI: 10.1364/OE.16.001460

[23] Yin GL, Lou SQ, Zou H. A multiwavelength Er-doped fiber laser using a nonlinear optical loop mirror and a twin-core fiber-based Mach-Zehnder interferometer. Laser Physics Letters. 2013; 10(4): 045103. DOI: 10.1088/1612-2011/10/4/045103

[24] Wang LW, Lou SQ, Chen WG, Li HL. A novel method of rapidly modeling optical properties of actual photonic crystal fibres. Chinese Physics B. 2010; 19(8): 084209. DOI: 10.1088/1674-1056/19/8/084209

[25] Huang WP. Coupled-mode theory for optical waveguides: an overview. Journal of the Optical Society of America A. 1994; 11(3): 963–983. DOI: 10.1364/JOSAA.11.000963

[26] Yin GL, Lou SQ, Wang X, Han B. Dual-wavelength erbium-doped fiber laser with tunable wavelength spacing using a twin core fiber-based filter. Journal of Optics. 2014; 16(5): 055404. DOI: 10.1088/2040-8978/16/5/055404

[27] Snyder AW. Coupled-mode theory for optical fibers. Journal of the Optical Society of America. 1972; 62(11): 1267–1277. DOI: 10.1364/JOSA.62.001267

[28] Digonnet M, Shaw HJ. Wavelength multiplexing in single-mode fiber couplers. Applied Optics. 1983; 22(3): 484–491. DOI: 10.1364/AO.22.000484

[29] Zou Y, Dong X, Lin G, Adhami R. Adhami R: Wide range FBG displacement sensor based on twin-core fiber filter. IEEE/OSA Journal of Lightwave Technology. 2012; 30(3): 337–343. DOI: 10.1109/JLT.2011.2181334

[30] Nagano K, Kawakami S, Nishida S. Change of the refractive index in an optical fiber due to external forces. Applied Optics. 1978; 17(13): 2080–2085. DOI: 10.1364/AO.17.002080

[31] Yin GL, Lou SQ, Lu WL, Wang X. A high-sensitive fiber curvature sensor using twin core fiber-based filter. Applied Physics B. 2014; 115(1): 99–104. DOI: 10.1007/s00340-013-5578-z

[32] Shao LY, Laronche A, Smietana M, Mikulic P, Bock WJ, Albert J. Highly sensitive bend sensor with hybrid long-period and tilted fiber Bragg grating. Optics Communications. 2010; 283(13): 2690–2694. DOI: 10.1016/j.optcom.2010.03.013

[33] Yin GL, Lou SQ, Hua P, Wang X, Han B. Tunable fiber laser by cascading twin core fiber-based directional couplers. IEEE Photonics Technology Letters. 2014; 26(22): 2279–2282. DOI: 10.1109/lpt.2014.2351808

[34] Yin GL, Lou SQ, Wang X, Han B. Tunable multi-wavelength erbium-doped fiber laser by cascading a standard Mach–Zehnder interferometer and a twin-core fiber-based filter. Laser Physics Letters. 2013; 10(12): 125110. DOI: 10.1088/1612-2011/10/12/125110